

Detailed CO ($J=1-0$, $2-1$ and $3-2$) observations toward an HII region RCW 32 in the Vela Molecular Ridge

Rei ENOKIYA¹, Hidetoshi SANO^{1,2}, Katsuhiro HAYASHI¹, Kengo TACHIARA¹,
Kazufumi TORII³, Hiroaki YAMAMOTO¹, Yusuke HATTORI¹, Yutaka HASEGAWA⁴, Akio
OHAMA¹, Kimihiro KIMURA⁴, Hideo OGAWA⁴ and Yasuo FUKUI¹

¹Department of Physics, Nagoya University, Chikusa-ku, Nagoya, Aichi 464-8601, Japan

²Institute for Advanced Research, Nagoya University, Furo-cho, Chikusa-ku, Nagoya 464-8601, Japan

³Nobeyama Radio Observatory, Minamimaki-mura, Minamisaku-gun, Nagano, 384-1305, Japan

⁴Department of Physical Science, Graduate School of Science, Osaka Prefecture University, 1-1
Gakuen-cho, Naka-ku, Sakai, Osaka 599-8531, Japan

*E-mail: enokiya@a.phys.nagoya-u.ac.jp

Received ; Accepted

Abstract

We made CO ($J=1-0$, $2-1$, and $3-2$) observations toward an HII region RCW 32 in the Vela Molecular Ridge. The CO gas distribution associated with the HII region was revealed for the first time at a high resolution of 22 arcsec. The results revealed three distinct velocity components which show correspondence with the optical dark lanes and/or H α distribution. Two of the components show complementary spatial distribution which suggests collisional interaction between them at a relative velocity of ~ 4 km s⁻¹. Based on these results, we present a hypothesis that cloud-cloud collision determined the cloud distribution and triggered formation of the early B star(s) ionizing RCW 32. The collision time scale are estimated from the cloud size and the velocity separation to be ~ 2 Myrs and terminated ~ 1 Myr ago, which is consistent with an age of the B star(s) and the associated cluster. By combining the previous works on the HII regions in the Vela Molecular Ridge, we argue that the majority, nearly ten, of the HII regions in the Ridge were formed by triggering in cloud-cloud collision.

1 Introduction

The Vela Molecular Ridge (VMR) was observed for the first time in the ^{12}CO ($J=1-0$) emission line by May et al. (1988). They found a huge molecular complex at distance of 0.4 – 2.0 kpc toward the Vela region and named as the Vela Molecular Ridge. This complex has total molecular mass of $\sim 10^5 M_{\odot}$ and was divided into four regions the VMR A, B, C and D by Murphy & May (1991). These authors compared stars whose distances were measured through photometric observations and concluded that the VMR A, C and D are located at 0.7 – 1.0 kpc while the VMR B at ~ 2.0 kpc. These distances agree with those derived through near infrared reddening by Liseau et al. (1992).

1.1 RCW 32

RCW 32 (Rodgers et al. 1960) also known as Gum 15 (Gum 1955) is the brightest HII region in the VMR D located in the north of the Vela SNR. It looks like the trifold nebula (M20) at optical wavelengths because of the thin dark lanes. In its vicinity the largest HII region in the VMR D, RCW 27 having a diameter of ~ 1.7 degrees is located (Figure 1). One of the dark lanes named DC261.5+0.9 or SL2 shows a heliocentric velocity of 22.4 km s^{-1} corresponding to $V_{LSR} = +6.3 \text{ km s}^{-1}$ as measured by CO ($J=2-1$), which is nearly consistent with the velocity of the exciting star (Brand et al. 1984). The exciting star is suggested HD 74804 (HIP 42908) of B0V or B4II (Pettersson & Reipurth 1994 and references therein) which is located in the center of a young star cluster Collinder 197 (Cr 197; Collinder 1931). Cr 197 with $\sim 660 M_{\odot}$ contains a few T-Tauri stars and 75 % of the members are pre-main sequence stars. The cluster is considered to be an on-going star forming site with an age of ~ 1 Myr (Pettersson & Reipurth 1994) or 5 ± 4 Myr (Bonatto & Bica 2010). Based on UBV photometrical observations (Fitzgerald et al. 1979), a ZAMS-fit of the cluster members (Vogt & Moffat 1973) and spectroscopic observations (Crampton & Fisher 1974) were made and distance of Cr 197 is measured to be 1.02, 1.05, and 0.72 kpc, respectively, by these authors; according to Pettersson & Reipurth (1994) the last small value could be explained if the stars are more luminous than Crampton & Fisher (1974) assumed. The cluster has another early B star CD-40 4579 which is measured to be B2V and is located 1.5 pc from its center. Yamaguchi et al. (1999) conducted ^{13}CO ($J=1-0$) observations toward 23 southern HII regions with bright-rimmed clouds (BRCs) and showed

that distribution of molecular clouds facing HII regions is strongly affected by UV radiation and forming massive stars possibly via radiation driven implosion (RDI). RCW 32 is accompanied by two BRCs SFO 57 and 58 (Sugitani & Ogura 1994). SFO 58 has a V-shaped appearance and is classified as an “A type” BRC by Sugitani et al. (1991). Urquhart et al. (2006) carried out ^{12}CO ($J=1-0$), ^{13}CO ($J=1-0$) and C^{18}O ($J=1-0$) observations toward SFO 58 by the Mopra 22m telescope and 3.6 cm and 6 cm radio continuum observations by the Australia telescope Compact Array (ATCA), and found that a ^{12}CO ($J=1-0$) cloud, which is located in the bright rim, accompanies an embedded ultracompact HII region excited by a single B2 – B3 star and a possible molecular outflow. The authors concluded that SFO 58 is strongly affected by HD 74804 and the ongoing star formation was triggered by RDI of HD 74804.

In the present paper, we report results of first multi- J transition CO line observations by the NANTEN2, Mopra and Atacama Sub-mm Telescope Experiment (ASTE) telescopes with resolutions of $22'' - 180''$ toward RCW 32 and discuss its formation mechanism through comparing distribution of CO and other wavelengths. We adopt a distance of 1.0 kpc for RCW 32. In Section 2, we describe our observations. Section 3 consists of four subsections; Subsections 3.1 and 3.2 present large- and small-scale gas distribution toward RCW 32 and in Subsections 3.3 and 3.4, we derive physical properties of CO gas in RCW 32. In Section 4, we discuss cloud-cloud collision as a possible formation mechanism of the exciting star of RCW 32 and give conclusions of the present study in Section 5.

2 Observations

2.1 ^{12}CO ($J = 1-0$) and ^{13}CO ($J = 1-0$)

^{12}CO ($J=1-0$) and ^{13}CO ($J=1-0$) datasets were observed by the NANTEN2 4-m mm/sub-mm telescope at Atacama, Chile in October 2011. The half power beam width (HPBW) of the NANTEN2 telescope at ~ 115 GHz corresponds to $\sim 180''$. The 4 K cooled Nb Superconductor–Insulator–Superconductor (SIS) double-side band (DSB) mixer receiver installed as the frontend enabled us to observe both the ^{12}CO ($J=1-0$) and ^{13}CO ($J=1-0$) lines simultaneously. The typical system noise temperatures toward RCW 32 including the atmosphere for ^{12}CO ($J=1-0$) and ^{13}CO ($J=1-0$) were ~ 200 and ~ 150 K, respectively. The backend consists of two Acqiris signal analyzers (AC240) as the digital Fourier transform spectrometer (DFS). Each DFS has 16384 channels with a 1 GHz band width and centered on 115.271202 GHz for ^{12}CO ($J=1-0$) and 110.201353 GHz for ^{13}CO ($J=1-0$) provided velocity coverages of $\sim 2600 \text{ km s}^{-1}$ and $\sim 2700 \text{ km s}^{-1}$ and velocity resolutions of $\sim 0.159 \text{ km s}^{-1}$ and $\sim 0.166 \text{ km s}^{-1}$, respectively. Observations were conducted by the on-the-fly (OTF) mode with Nyquist Sampling and two orthogonal scan maps (an x scan map and a y scan map) with 1.0 degree by

1.0 degree were summed up to reduce scanning effects. We used the spectrum of $(l, b) = (262.^{\circ}4000, 1.^{\circ}8001)$, which has no significant emission at 0.25 K (T_a^*) sensitivity, as the reference spectrum for the blank sky. The pointing accuracy was checked every 2 hours and was achieved to be within 10 through cross scan observations of IRC+10216 or the sun. The absolute intensity calibration was done through comparing peak intensity of Orion-KL [$\alpha_{J2000} = 5^h35^m14.^s48$, $\delta_{J2000} = -5^{\circ}22'27''.55$] observed by NANTEN2 (Ridge et al. 2006).

2.2 $^{12}\text{CO}(J=2-1)$ and $^{13}\text{CO}(J=2-1)$

$^{12}\text{CO}(J=2-1)$ and $^{13}\text{CO}(J=2-1)$ datasets were obtained by NANTEN2 from November 4 to 8 in 2015. The HPBW of the NANTEN2 telescope at ~ 230 GHz corresponds to ~ 90 . The 4 K cooled Nb SIS DSB mixer receiver installed as the frontend enabled us to observe both $^{12}\text{CO}(J=2-1)$ and $^{13}\text{CO}(J=2-1)$ lines simultaneously. The typical system noise temperature toward RCW 32 including the atmosphere for both lines was ~ 140 K. The backend configuration is the same as $\text{CO}(J=1-0)$ observations but the DFS centered on 230.538000 GHz for $^{12}\text{CO } J=2-1$ and 220.398681 GHz for $^{13}\text{CO } J=2-1$ provided velocity coverages of $\sim 1300 \text{ km s}^{-1}$ and $\sim 1350 \text{ km s}^{-1}$ and velocity resolutions of $\sim 0.080 \text{ km s}^{-1}$ and $\sim 0.083 \text{ km s}^{-1}$, respectively. Observations were conducted by the OTF mode with Nyquist Sampling and orthogonal two scan maps (an x scan map and a y scan map) with 30 arcmin by 30 arcmin were summed up to reduce scanning effects. We used the spectrum of $(l, b) = (262.^{\circ}3708, 1.^{\circ}2347)$, which has no significant emission in 0.12 K (T_a^*) sensitivity, as the reference spectrum for the blank sky. The pointing accuracy was checked every 4 hours and was achieved to be better than 10 through cross scan observations of IRC+10216. The absolute intensity calibration was done through pixel-by-pixel comparisons between two OTF maps with resolution of $204''$ toward Orion B obtained with NANTEN2 and 1.85-m telescope by Osaka Prefecture University (Onishi et al. 2013; Nishimura et al. 2015). We use $28'$ by $28'$ maps corresponding to 28 pixels by 28 pixels centered on $(l, b) = (206.^{\circ}45, -16.^{\circ}33)$ with integrated velocity range from 1.7 to 15.7 km s^{-1} . Correlation coefficients derived from these data were 1.28 for $^{12}\text{CO}(J=2-1)$ and 1.24 for $^{13}\text{CO}(J=2-1)$. The peak intensity in the calibrated map for each line was 149 K km s^{-1} for $^{12}\text{CO}(J=2-1)$ toward $(l, b) = (206.^{\circ}41, -16.^{\circ}26)$ and 58 K km s^{-1} for $^{13}\text{CO}(J=2-1)$ toward $(l, b) = (206.^{\circ}56, -16.^{\circ}36)$.

2.3 $^{12}\text{CO}(J=3-2)$

$^{12}\text{CO}(J=3-2)$ datasets were observed by the ASTE 10 m sub-mm telescope at Atacama, Chile from November 29 to December 5 in 2016 (Ezawa et al. 2004; 2008). The HPBW of the ASTE telescope

at ~ 345 GHz corresponds to $\sim 22''$. A cartridge-type dual-polarization side-band separating mixer receiver for the 350 GHz band, “DASH 345“, was used for the observations. The typical system noise temperature toward RCW 32 including the atmosphere was ~ 300 K. Two XF-type digital spectro-correlators, “MAC“ with the narrow band mode (bandwidth = 128 MHz) centered on 345.795990 GHz which provided a velocity coverage of ~ 111 km s $^{-1}$ and velocity resolution of ~ 0.11 km s $^{-1}$ were selected for the observations (Sorai et al. 2000). Our observations were conducted by the OTF mode with Nyquist Sampling and orthogonal two scan maps (an x scan map and a y scan map) with 8.0 arcmin by 8.0 arcmin were summed up to reduce scanning effects. We used the spectrum of $(l, b) = (262^\circ 46, 1^\circ 71)$, which has no significant emission in 0.12 K (T_a^*) sensitivity, as the reference spectrum for the blank sky. The pointing accuracy was checked every 2 hours and was achieved to be within $3''$ through cross scan observations of RAFGL 4078 (07h45m02.41s, $-71^\circ 19' 45.7''$) and GX Mon (06h52m47.04s, $+08^\circ 25' 18.8''$). The absolute intensity calibration was done by comparing peak intensity of IRC+10216 [$\alpha_{\text{B1950}} = 9^{\text{h}}45^{\text{m}}14.^{\text{s}}8$, $\delta_{\text{B1950}} = -13^\circ 30' 40''$] observed by the ASTE telescope and the CSO telescope to be 32.5 K (Wang et al. 1994).

3 Results

3.1 Gas Distributions in the vicinity of RCW 32

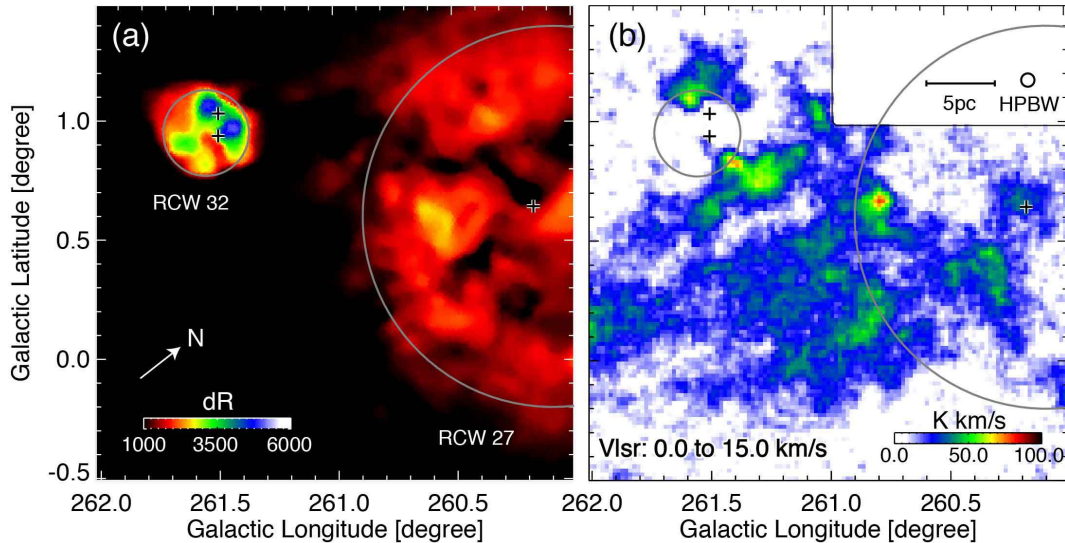


Fig. 1. Large-scale molecular / ionized gas distributions of RCW 32. The small and large gray circles indicate the size of RCW 32 and 27 respectively. The cross in RCW 27 indicates the position of the exciting star and crosses in RCW 32 indicate positions of early B stars associated with RCW 32. (a) Distribution of the H α recombination line emission obtained by smoothed continuum-subtracted image of the Southern H-Alpha Sky Survey Atlas (SHASSA; Gaustad et al. 2001). (b) Integrated intensity distribution of the ^{12}CO ($J=1-0$) with velocity integration range of 0.0 to 15.0 km s $^{-1}$ obtained by the NANTEN2 telescope.

Figure 1 shows large-scale distributions of the molecular and ionized gas toward RCW 32

in a 2 degree by 2 degree field. Figure 1a shows distribution of the H α recombination line emission (Gaustad et al. 2001). The small and large gray circles indicate approximate extent of RCW 32 and RCW 27, respectively. Crosses show positions of early B stars (CD-40 4579 and HD 74804) in RCW 27 and the exciting star (HD 73882) of RCW 32. In H α RCW 32 is more than twice as bright as RCW 27. The elongated depression from the center of RCW 32 to the west corresponds to the dark lane SL2 (Brand et al. 1984). Figure 1b shows velocity integrated intensity distribution of ^{12}CO ($J=1-0$) observed by the NANTEN2 telescope, where the integrated velocity range is from 0.0 to 15.0 km s $^{-1}$. The molecular gas is extended over the region and there is an anti-correlated distribution between CO and H α toward RCW 32.

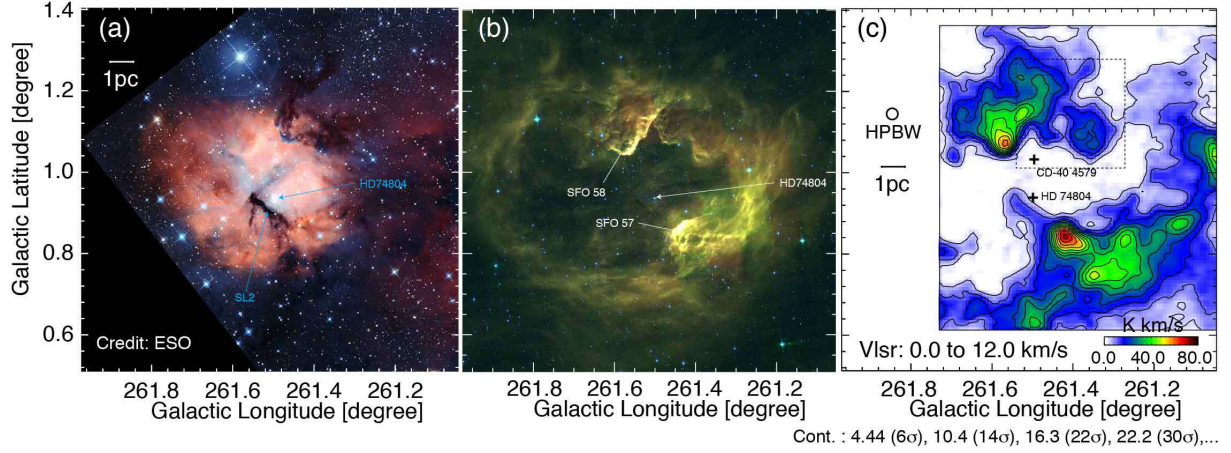


Fig. 2. RCW 32 in various wavelengths. (a) Optical three-color composite image of RCW 32. Blue, yellow, and red correspond to B band, R band, and H α taken by the MPG/ESO 2.2-metre telescope (credit: ESO). (b) Infrared three-color composite image of RCW 32. Blue, green, and red correspond to 3.6, 5.8, and 8.0 μm obtained by GLIMPSE (Benjamin et al. 2003, Churchwell et al. 2009). (c) Integrated intensity distribution of the ^{12}CO ($J=2-1$) obtained by the NANTEN2 telescope. The dashed square shows the region which we observed in ^{12}CO ($J=3-2$) with the ASTE telescope. Crosses indicate positions of early B stars of CD-40 4579 and HD 74804 in this region.

Figure 2 shows close-up views toward RCW 32 at optical and infrared wavelengths and the CO distribution. Figure 2a shows an optical three composite color image of RCW 32 obtained by Wide Field Imager installed at MPG / ESO 2.2-metre telescope in La Silla, Chile (Credit: ESO¹). The red, green, and blue represent H α , R band, and B band, respectively. The HII region RCW 32 is roughly spherically with a radius of ~ 3 pc centered on the exciting star HD 74804, and the star cluster Cr 197 including HD 74804 spreads with a radius of 1.5 pc centered on the star. The dark lane SL2 is seen from the center of RCW 32 to the west clearly. Figure 2b shows an infrared three composite color image² of RCW 32 obtained with the *Spitzer space telescope*. The red, green, and blue represent distributions at 8.0, 5.8, and 3.6 μm , respectively. The figure shows that the dust emission at the

¹ <https://www.eso.org/public/images/eso1420c/>

² <http://irsa.ipac.caltech.edu/data/SPITZER/GLIMPSE/overview.html>

infrared wavelengths delineates the outer boundary of RCW 32 in particular on the west.

In Figure 2b the two bright features in the north and south correspond to the BRCs SFO57 and SFO58. The exciting star HD 74804 is located in the center of RCW 32 between these BRCs. The bright rim delineates the western edge of SFO58. The dark lane SL2 is not seen in the infrared wavelength. Figure 2c shows integrated intensity distribution of ^{12}CO ($J=2-1$) observed with NANTEN2 with the integrated velocity range from 0.0 to 12.0 km s $^{-1}$. The black crosses indicate the positions of stars earlier than B4. The dashed black box indicates the region where we observed in ^{12}CO ($J=3-2$) with ASTE. Figure 2c shows that the two peaks of the molecular clouds are distributed toward the two BRCs. The dense molecular cloud toward SFO 58 exhibits an active on-going young massive star formation as shown by the infrared object IRAS08435-4105. We find that SL2, SFO 57, SFO 58 and the western rim feature of SFO 58 have their accompanying molecular clouds. The northeastern part of the infrared ellipsoidal boundary seen in Figure 2b seems to be associated with the diffuse molecular cloud. The distribution of the overall molecular gas implies that RCW 32 is not a young HII region, where molecular gas inside of the HII region is almost fully ionized by the exciting star except for the two BRCs which still hold their original cloud shape at least in part.

Figure 3 shows velocity-channel distribution of the ^{12}CO ($J=2-1$) emission superposed on the optical composite image of Figure 2a. The black crosses indicate positions of the two early B stars. In a velocity range from 1.4 to 3.8 km s $^{-1}$, the molecular cloud (hereafter the blue cloud) corresponds to the dark cloud and the weak molecular emission corresponds to the dark spot in the south of RCW 32 around $(l, b) = (261^\circ.68, 0^\circ.80)$. In a velocity range from 2.6 to 6.8 km s $^{-1}$, the molecular cloud (hereafter the red cloud West) corresponds to SFO 57 and a V-shaped molecular cloud (hereafter the red cloud East) corresponds to SFO 58. In a velocity range from 3.2 to 5.6 km s $^{-1}$, a large molecular cloud with a size of ~ 5 pc corresponds to the dark cloud in the northwest of RCW 32. The cloud shows no strong sign of interaction with the B stars. In a velocity range from 5.6 to 7.4 km s $^{-1}$, the molecular cloud corresponds to SL2 (hereafter SL2 cloud).

Figure 4 shows ^{12}CO ($J=2-1$) contours of the four clouds (the red cloud West, the red cloud East, the blue cloud, and the SL2 cloud) superposed on a three color composite image as shown in Figures 2a and 2b. Black crosses indicate positions of two early B stars. Figure 2a shows that the red clouds are brightest in CO, having higher hydrogen column density of 6×10^{21} cm $^{-2}$, than the other clouds, whereas the SL2 cloud has the lowest column density. In Figure 4a the red cloud East and West, the highest column density clouds in the four, are not dark in the optical wavelength and luminous in the infrared wavelength. This indicates that these two clouds are not on the near side of the HII region RCW 32. On the other hand, the blue and SL2 clouds are dark in the optical wavelength and should be located in front of RCW 32. Figure 4b shows complementary spatial

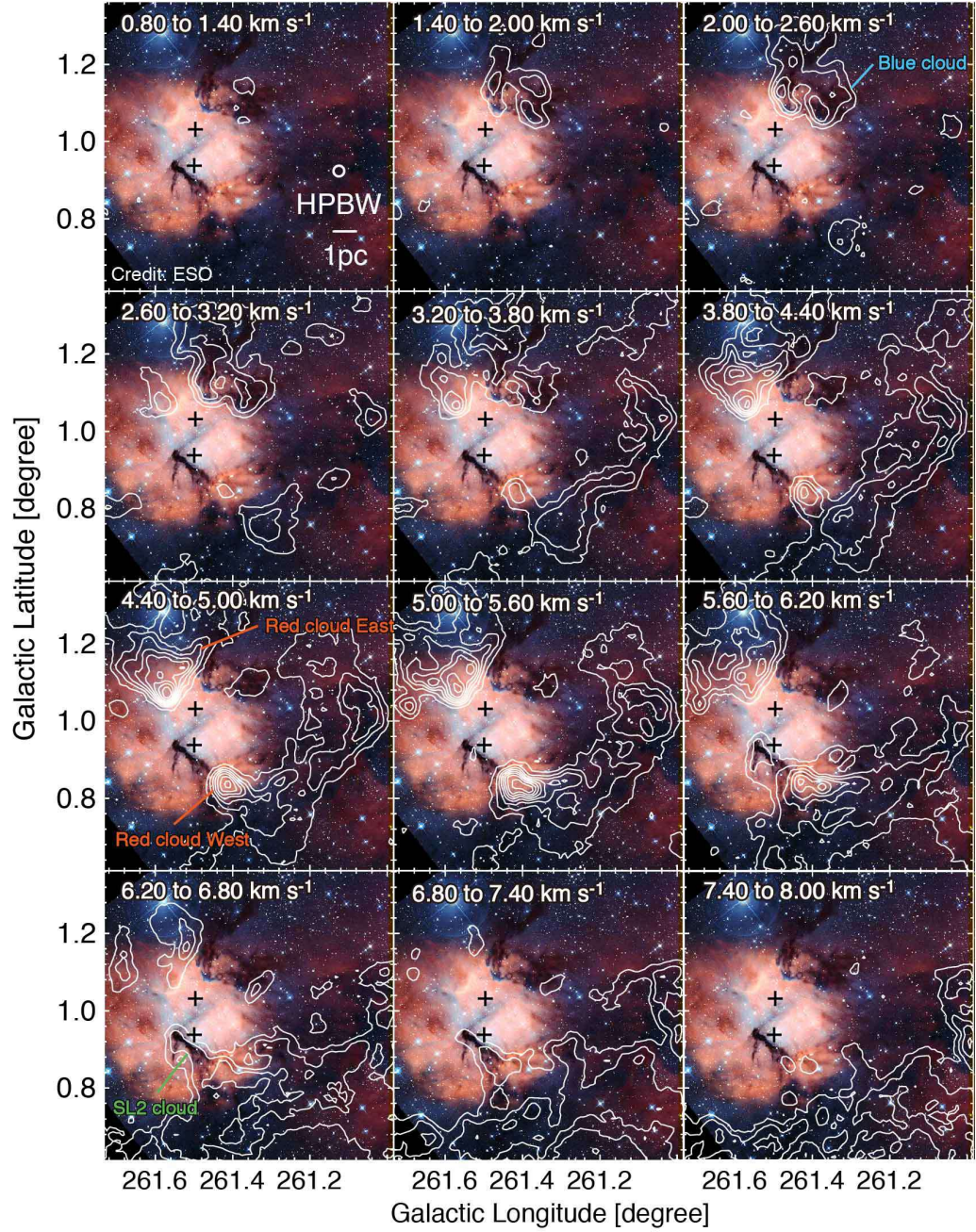


Fig. 3. Velocity channel distribution of ^{12}CO ($J=2-1$) superposed on the optical image of Figure 2a (Credit: ESO). Contours are from 2.1 Kkm s $^{-1}$ with the step of 3.37 Kkm s $^{-1}$. Velocity integration ranges are shown at the top of each panel.

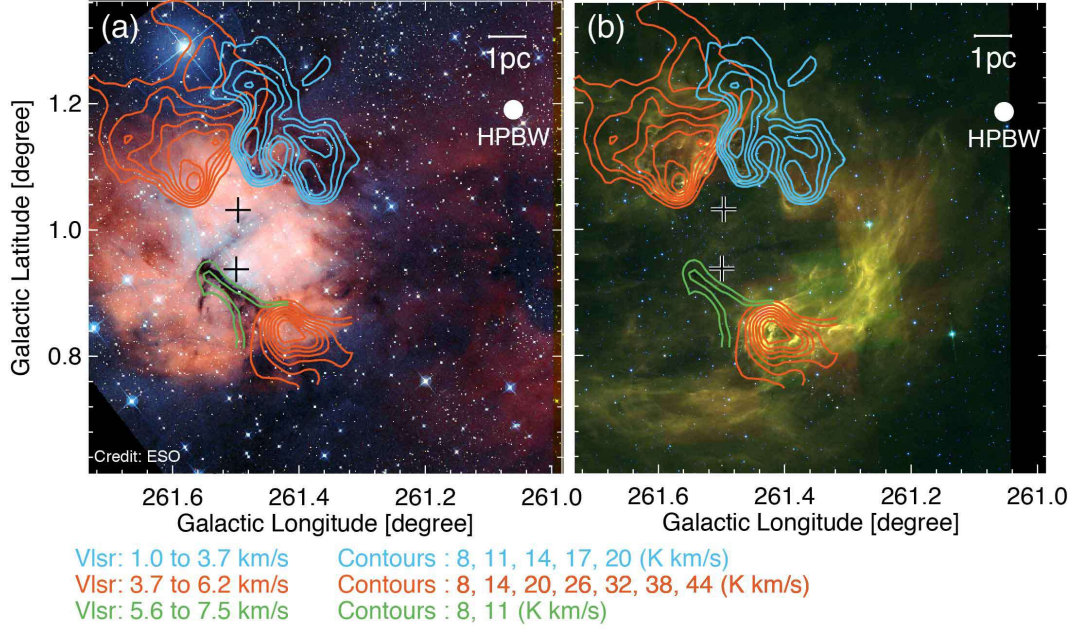


Fig. 4. Integrated intensity distributions of ^{12}CO ($J=2-1$) corresponding to red (red contours), blue (blue contours), and SL2 clouds (green contours) superposed on (a) the optical and (b) infrared images.

distribution between the red cloud East and the blue cloud while the two clouds have distinct radial velocity and distance. The shape of the blue cloud and its infrared ridge suggests that the cloud is dynamically affected by the B stars.

3.2 Detailed Molecular Distribution of Red and Blue Clouds

Figure 5 shows velocity channel distribution of the ^{12}CO ($J=3-2$) emission obtained with ASTE superposed on three optical color composite image of the Figure 2a. The black crosses indicate the positions of the early B star CD-40 4579. Dark clouds in $l = 261.^\circ45 - 261.^\circ50$, $b = 1.^\circ07 - 1.^\circ15$ are influenced by the UV radiation from the B star and exhibit a pillar-like structure like as seen in *the pillars of creation* in the Eagle nebula (M16). The $J=3-2$ transition data with a finer spatial resolution clearly show elongated filamentary molecular clouds in the blue cloud. In a velocity range from 0.8 to 5.6 km s^{-1} , the blue cloud corresponds to the optical dark cloud. The shape of the blue cloud indicates that the cloud is influenced by CD-40 4579. In another velocity range from 3.8 to 6.2 km s^{-1} , the red cloud East is distributed along the eastern edge of the blue cloud. In the other velocity range from 5.6 to 6.2 km s^{-1} , another the red cloud East is distributed along the western edge of the blue cloud.

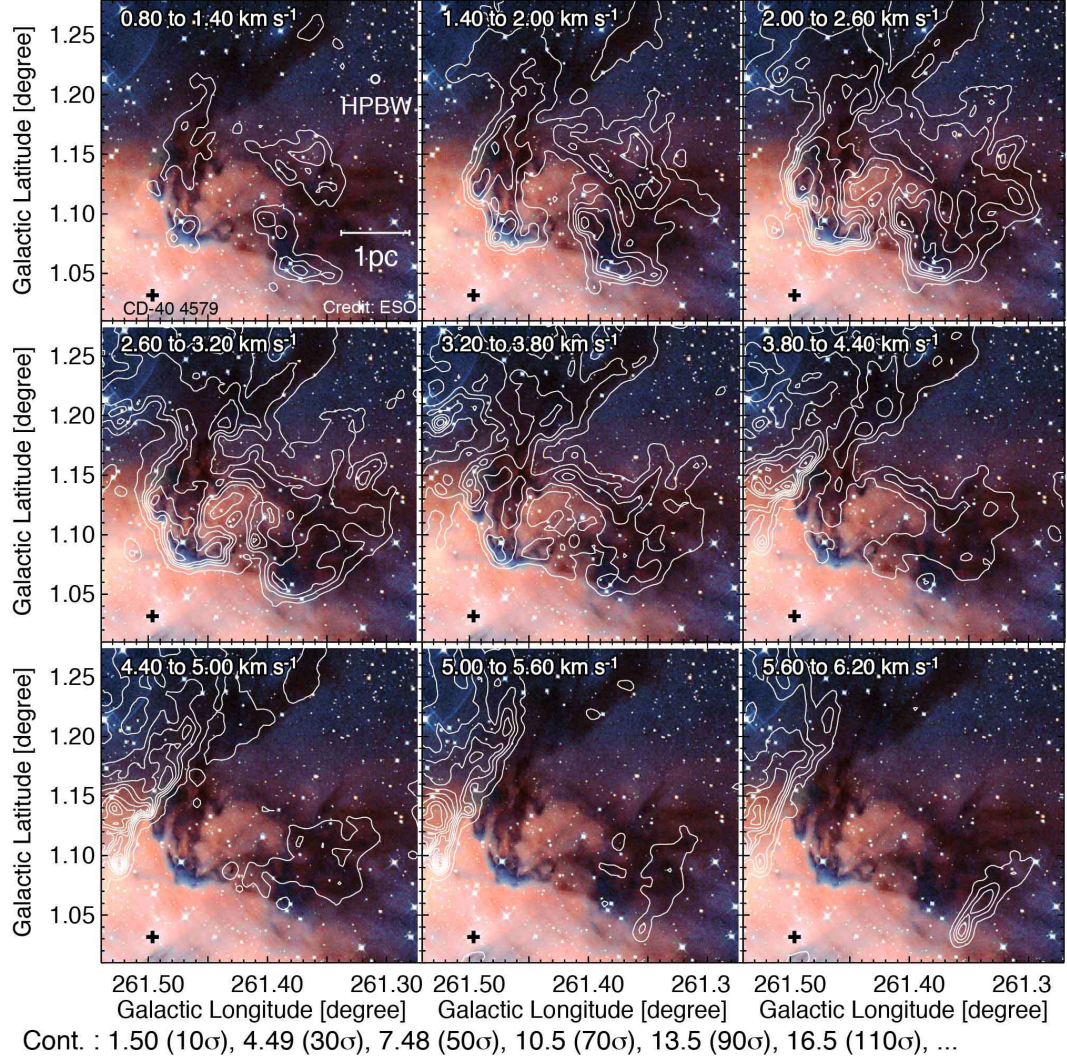


Fig. 5. Velocity channel distribution of ^{12}CO ($J=3-2$) obtained by the ASTE telescope superposed on the optical image of figure 2a (Credit: eso).

3.3 Intensity ratio of $^{12}\text{CO} J = 3-2 / 2-1$

Figure 6 shows velocity channel distribution of a intensity ratio $R_{3-2/2-1}$ between the ^{12}CO ($J=3-2$) emission and the ^{12}CO ($J=2-1$) emission. We used the pixels with intensities higher than three sigmas for the both data. Contours show the integrated intensity of the ^{12}CO ($J=2-1$) emission. The black crosses indicate the positions of the early B star CD-40 4579. The typical value of $R_{3-2/1-0}$ and $R_{2-1/1-0}$ for molecular clouds in the Galactic disk is estimated to be ~ 0.4 and ~ 0.5 , respectively, from Figure 4 in Oka et al. (2012) and Figure 10c in Enokiya et al. (2014a). We thus estimate the typical value of $R_{3-2/2-1}$ for disk clouds to be $0.4 / 0.5 = 0.8$. In the velocity from 0.8 to 3.8 km s^{-1} , the blue cloud exhibits a gradient in $R_{3-2/2-1}$ toward CD-40 4579 and the inner part of the blue cloud facing to CD-40 4579 shows $R_{3-2/2-1}$ higher than 1.0 up to 1.6, whereas the outer part of the cloud shows $R_{3-2/2-1}$ lower than 0.8. This suggests that the blue cloud is associated with CD-40 4579 and

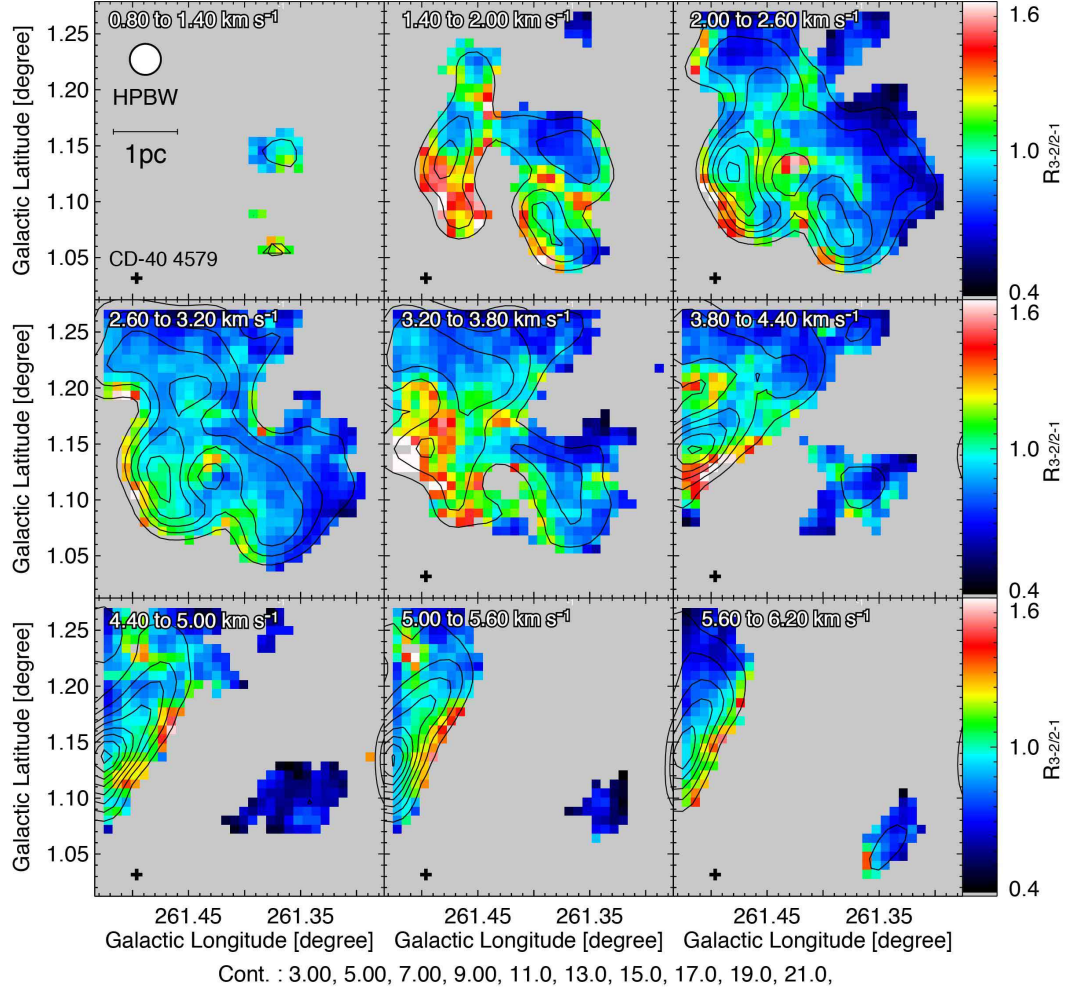


Fig. 6. Velocity channel distribution of ratio of ^{12}CO ($J=3-2$) / ^{12}CO ($J=2-1$). Contours show distribution of integrated intensity of ^{12}CO ($J=2-1$).

is heated up radiatively. In a velocity from 3.8 to 6.2 km s^{-1} , the red cloud East shows a gradient of $R_{3-2/2-1}$ toward its sharp edge and very high $R_{3-2/2-1}$ over 1.5 are seen on the edge. The edge corresponds to SFO 58 and its exciting star source is another early B star HD 74804 (Urquhart et al. 2006). In a velocity range from 3.8 to 5.6 km s^{-1} , the cloud, a possible part of the blue cloud at $(l, b) \sim (261.35, 1.10)$, shows a ratios of typical value for the Galactic disk and is not significantly affected by the B stars. In a velocity from 5.6 to 6.2 km s^{-1} , the cloud, a possible part of the red cloud East at $(l, b) \sim (261.35, 1.05)$, show a gradient of a ratio toward CD-40 4579 and show significantly high values (0.9 to 1.3) at the closest region to CD-40 4579.

3.4 Physical Parameters of the Molecular Clouds

In this subsection, we derive physical parameters such as molecular mass and column density for each cloud. Molecular mass M in M_{\odot} is estimated from Equations (1).

$$M = \mu m_p \sum_i [d^2 \Omega N_i(\text{H}_2)] \quad (1)$$

where μ , m_p , d , Ω and $N_i(\text{H}_2)$ are mean molecular weight, mass of hydrogen, distance, solid angle of a pixel, and column density of molecular hydrogen for i -th pixel, respectively. We use 20 % for abundance of helium corresponding μ is 2.8 and 1.0 kpc for the distance. Column densities of molecular hydrogen for each cloud is estimated by Equation (2).

$$N(\text{H}_2) = X \times W(^{12}\text{CO}) \quad (2)$$

where $W(^{12}\text{CO})$ is integrated intensity of ^{12}CO ($J=1-0$) and X is an empirical conversion factor from $W(^{12}\text{CO})$ to $N(\text{H}_2)$. We adopt $X = 1.0 \times 10^{20} \text{ cm}^{-2} (\text{K km s}^{-1})$ which is derived by Okamoto et al. (2017) by using the *Planck* dust emission data toward the Perseus molecular cloud. From these equations, molecular masses for the blue cloud, the red cloud East and the red cloud West are derived as 360, 900, and $300 M_\odot$ and maximum column densities are $\sim 2 \times 10^{21}$, $\sim 6 \times 10^{21}$, and $\sim 6 \times 10^{21} \text{ cm}^{-2}$, respectively. Detailed physical parameters for each cloud are summarized in Table 1.

Table 1. Physical parameters of the molecular clouds

Cloud name	V_{LSR} [km s $^{-1}$]	Peak Velocity [km s $^{-1}$]	Molecular mass [M_\odot]	$N(\text{H}_2)$ [cm $^{-2}$]
blue cloud	1.4 – 3.8	2.8	400	2×10^{21}
red cloud East	2.6 – 6.8	5.2	900	6×10^{21}
red cloud West	2.6 – 6.8	5.4	300	6×10^{21}
SL2 cloud	5.6 – 7.4	6.3	60	1×10^{21}

Note. — Col.1: Cloud's name. Col.2 Velocity span derived from ^{12}CO ($J=2-1$) dataset. Col.3 Peak velocity derived from a gaussian fit of an average profile of each clouds in ^{12}CO ($J=2-1$). Col.4 Molecular mass. Col.5 Maximum molecular column density $N(\text{H}_2)$ toward each cloud.

4 Discussion

4.1 Molecular distribution

We summarize the present observational results as follows;

1. Molecular clouds toward RCW 32 are distributed in four different components, the blue cloud, the red cloud East, the red cloud West and the SL2 cloud.
2. The red cloud West, corresponding to SFO 57, has $V_{LSR} = 2.6 - 6.8 \text{ km s}^{-1}$ and $360 M_\odot$. The red cloud East, corresponding to SFO 58, has $V_{LSR} = 2.6 - 6.8 \text{ km s}^{-1}$ and $900 M_\odot$. The blue cloud with $V_{LSR} = 1.4 - 3.8 \text{ km s}^{-1}$ and $300 M_\odot$ has a counterpart in the optically dark features in the northwest of RCW 32. The SL2 cloud at $5.6 - 7.4 \text{ km s}^{-1}$ corresponds to the central dark lane SL2.

3. The blue cloud stuck to the near side to us of RCW 32 while the red cloud East and West locate interior of RCW 32.
4. We found complementary spatial distribution between the red cloud East and the blue cloud which suggests their physical connection, while these two clouds have different radial velocity by $\sim 2.4 \text{ km s}^{-1}$.
5. Both the red and blue clouds have regions with a ratio $R_{3-2/2-1}$ over 1.2 which is substantially higher as compared with the typical value in Galactic disk clouds (~ 0.8).

4.2 Parent Cloud(s) of the Star Cluster Cr 197

Figure 2a suggests that RCW 32 is not a young HII region because the central B stars are not associated with the parent clouds within $\sim 1 \text{ pc}$. It is likely that the molecular gas has been dispersed by ionization and winds from the two early B type stars. There is no work which addressed the formation of the B stars. The present results on detailed molecular distribution opened a possibility to access the formation mechanism. We found that the two red clouds in East and West have similar ranges of radial velocities, peak velocities, and column densities. Furthermore, it is probable that both of them are ionized by the same source (HD74804) and form bright rims toward the side close to the ionization source (see Figure 3 and Table 1). This suggests that the two red clouds had been an unified large cloud which is distributed from direction of the red cloud East to West until B stars were formed. The blue cloud also has a possible separated part which shows almost the same magnitude of extinction as the blue cloud (see Figure 3) across the opposite side of the ionization source at $(l, b, v) = (261.^\circ 68, 0.^\circ 8, 1.4 - 3.8 \text{ km s}^{-1})$. Thus, it is possible to consider both the red and blue clouds as natal clouds of RCW 32.

4.3 Possible Origin of High Mass Stars

First, we examine a possibility of a simple model that the B stars were formed in the red or blue cloud in the past and the expanding motion was caused by the stellar wind which caused the observed velocity span between the red and blue clouds. Total mass of associated clouds is calculated to be $\sim 1600 M_\odot$.

The required mass to gravitationally bind the two clouds with a relative velocity of 4 km s^{-1} and a radius of 4.5 pc is calculated as $1.6 \times 10^4 M_\odot$. This value is an order of magnitude higher than the mass of clouds and the cluster itself, and thus the red and blue cloud are gravitationally unbound. Then, the mass of the two northern clouds (the red cloud East and the blue cloud) is 900 and $400 M_\odot$ respectively, and the required momentum to move these two clouds with a relative velocity of 4

km s^{-1} is calculated as $\sim 1 \times 10^3 M_{\odot} \text{ km s}^{-1}$. This value is almost the same with the analytical solution of momentum of O type star's stellar wind ($\sim 2 \times 10^3 M_{\odot} \text{ km s}^{-1}$; c.f., Abbott 1982a, b). If we take into account a loss of momentum, it is impossible to realize $\sim 1 \times 10^3 M_{\odot} \text{ km s}^{-1}$ by only two early B stars. Moreover, it is obvious that this kind of spherical expansion model hardly explain the complimentary distribution between the red and the blue cloud seen in Figures 4, 5, and 7. Because of these difficulties, we argue that the velocity span is hardly explained as due to the stellar wind. We next examine the possibility of a cloud-cloud collision as an alternative model.

4.4 Cloud-Cloud Collision as a Triggering Mechanism of High-Mass Star Formation

It was discussed that cloud-cloud collision (hereafter CCC) is a triggering mechanism of star burst activities in colliding galaxies (e.g., Young et al. 1986). Recent studies indicate that CCC phenomena frequently take place not only in interacting galaxies but also among molecular clouds in the Galaxy. Dobbs et al. (2015) carried out hydrodynamical numerical simulations of isolated galaxies and found that collisions of molecular clouds having a size larger than 10 pc occur every 8 – 10 Myr. The mean free time between collisions is sufficiently shorter than a life time of molecular clouds in a galaxy, ~ 20 Myrs (Fukui et al. 2008; Kawamura et al. 2009; Fukui and Kawamura 2010). Theoretically, Inoue & Fukui (2013) demonstrated that CCC realizes a large mass accretion rate of $\geq 10^{-4} - 10^{-3} M_{\odot} \text{ yr}^{-1}$ through three-dimensional magnetohydrodynamics (MHD) simulations, and that the high mass accretion rate leads to form massive, gravitationally bound molecular cloud cores, precursors of high mass stars. Habe & Ohta (1992) and Anathpindika (2009) showed that a collision between two molecular clouds with supersonic relative velocities generates a compressed layer at the collisional front, and that enhanced turbulence in the layer increases an effective sound speed and then increase the Jeans mass. Recent observations presented evidence on CCC in super star clusters (e.g., Westerlund 2, Furukawa et al. 2009; NGC3603, Fukui et al. 2013) and Galactic open clusters/HII regions (e.g., M20; Torii et al. 2011, RCW 120; Torii et al. 2015). These authors discovered two natal molecular clouds with various signatures of collision toward the young high mass stars. Three HII regions RCW 34, RCW 36, and RCW 38 in Vela C are also proposed as sites where CCC occurred and triggered the formation of O/early B stars (Sano et al. 2017, Hayashi et al. 2017; Fukui et al. 2016). These authors discovered that the two natal clouds exhibit complementary spatial distribution, an observational signature of collision (Fukui et al. 2018). It is therefore important to explore if CCC is a dominant mechanism in the VMR, and RCW 32 ionized by Cr 197 and the B stars is an obvious object in the test.

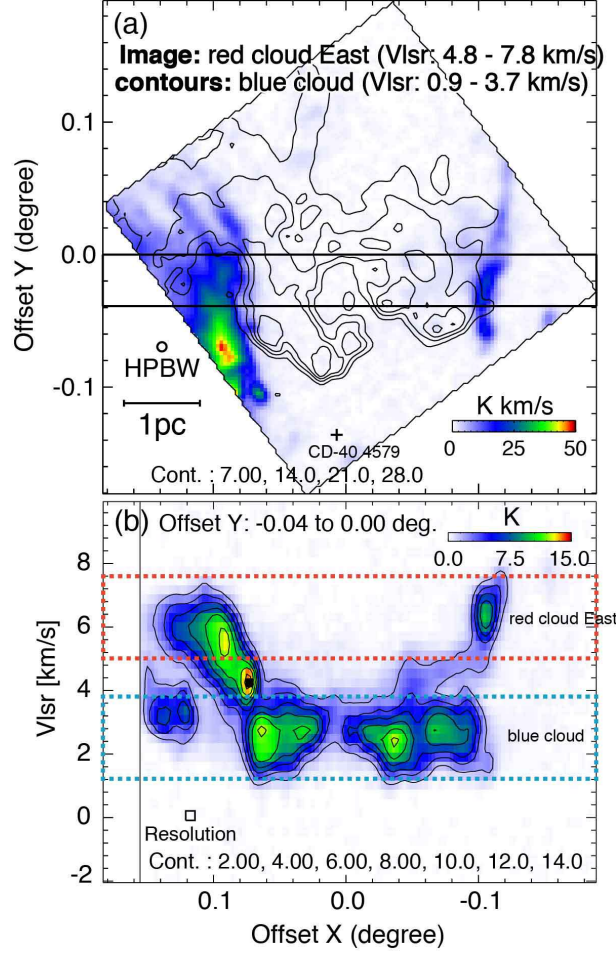


Fig. 7. (a) Integrated intensity distribution of red cloud (image) and blue cloud (contours) in ^{12}CO ($J=3-2$) in Offset X and Y coordinate. The integration ranges for red and the blue clouds are shown in the figure. The cross indicates the position of CD-40 4579. (b) Position-Velocity diagram of ^{12}CO ($J=3-2$) in Offset X and Y coordinate. The integration range is shown as the black box in Figure a.

Figure 7 shows a spatial distribution and position-velocity diagram of ^{12}CO ($J=3-2$) obtained with ASTE. The coordinate in the figure is taken along the direction of contact surfaces of blue and red cloud East. We defined the Offset X and Y axes by rotating l and b counterclockwise by 35 degree around $(l, b) = (261^\circ 40', 1^\circ 145')$. Figure 7a shows integrated intensity distribution of the red cloud (image) and the blue cloud (contours) in ^{12}CO ($J=3-2$), and indicates that two clouds show complementary distribution. Figure 7b shows a position (offset X)-velocity diagram toward the blue and red cloud East, and indicates that the two clouds have connecting bridge features at $4 - 5 \text{ km s}^{-1}$ on the both edges of the blue cloud. An integrated range in offset Y is shown in the black box in Figure 7a. The figure also shows bridge features toward the contact surfaces of them. This might be evidence of the past interaction between the two clouds. Since the complementary spatial distribution

in Figures 7a and 7b do not exhibit a displacement, both the clouds should not have any velocities toward the direction perpendicular to the line of sight and it should have been a head-on collision in the line of sight direction. The line intensity ratio and the BRCs provide unmistakable signs of physical association and interaction with the B stars. We also note that shock heating by collisional interaction is possible in the southeastern edge of the blue cloud which shows high line ratio not facing the B stars.

4.5.1 Signatures of collision

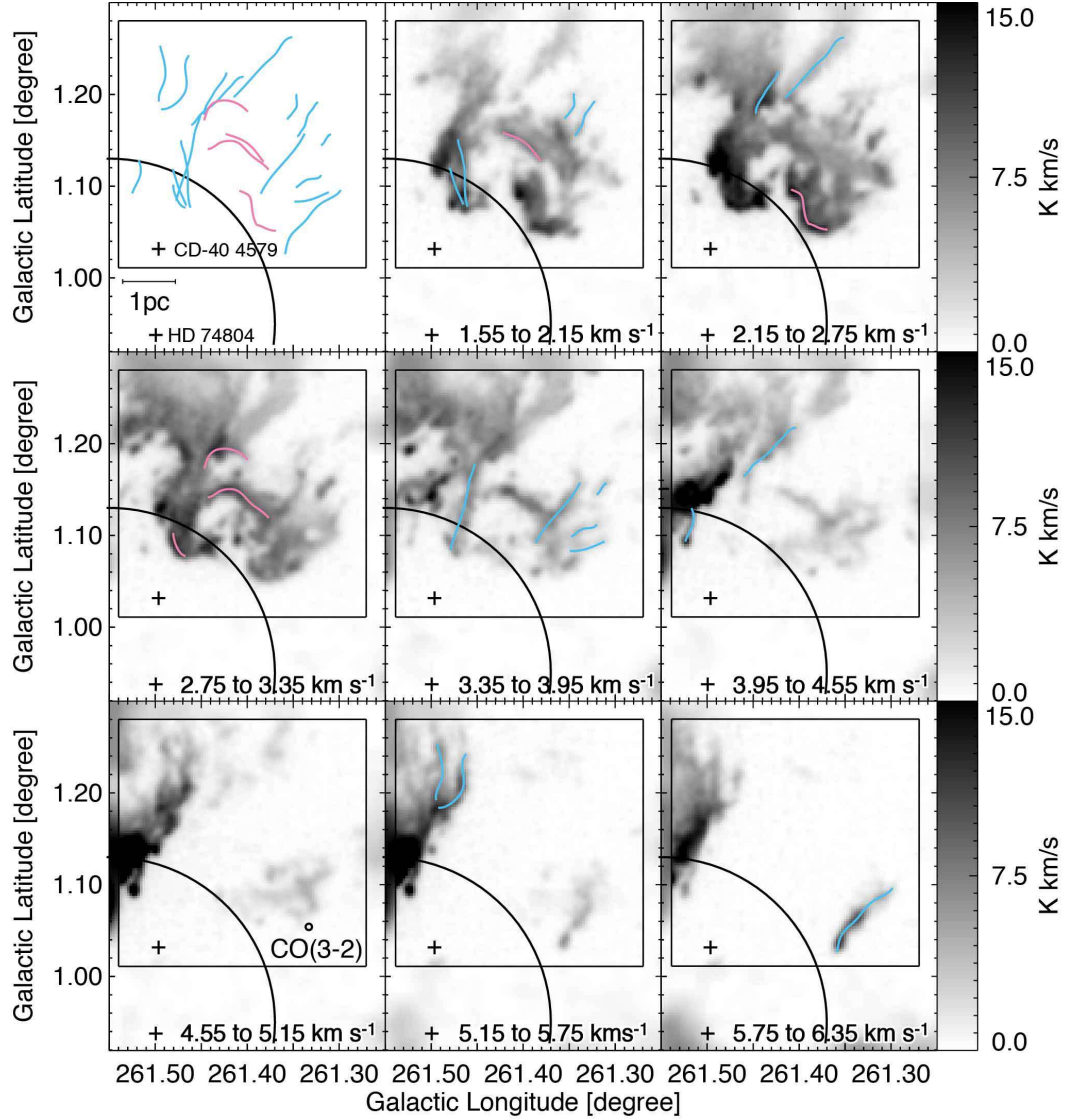


Fig. 8. Velocity channel distribution of composite CO data. The CO data consist of ^{12}CO ($J=3-2$) (inside the black box) and ^{12}CO ($J=2-1$) (remaining area) with independent resolutions. The black circle indicates the same circle in Figure 1 corresponds to the size of RCW 32. Cyan and purple lines show filamentary CO structures fitted by eyes. The left-top panel shows distribution of all filamentary molecular clouds defined here.

Figure 8 shows more detailed velocity channel distributions toward the blue cloud observed

with ASTE at a resolution of 22 arcsec in the ^{12}CO ($J=3-2$) transition. It is remarkable that the distribution is highly filamentary. We defined by eye inspection about 20 filaments as shown in Figure 8, where the filaments in cyan are normal to the boundary of the HII region and the other filaments are shown in purple. The filaments in purple are nearly along the boundary or along the southern edge of the blue cloud. The figure shows that some filaments in cyan are distributed sectorally and face to the direction of the B stars whereas the other filaments are distributed parallel to each other. It is plausible that such parallel filaments are formed accompanying star formation activities unrelated to UV radiation. These filamentary molecular structures are observed in some places where CCC took place and the authors discussed relation to CCC (N159 in LMC; Fukui et al. 2015, RCW 79; Fukui et al. 2017 in prep.). Furthermore Inoue & Fukui (2013) performed 3D MHD simulations of CCC and found that dense filamentary molecular clouds are formed through CCC by an anisotropic compression along magnetic field lines. The formation mechanism of the filaments is still unclear and ALMA observations of RCW 32 where molecular clouds locate within 1 kpc of the southern sky would be a key to understand it. The discussion above may lend support for the formation of Cr 197 and the B stars through CCC.

4.5.2 Possible scenario of cloud-cloud collision

The complementary spatial distribution between two clouds of different velocity is a signature of collisional interaction between them (Fukui et al. 2018), and the bridge feature between them is another signature of collision. If we adopt cloud-cloud collision to explain the cloud distribution and kinematics in RCW 32, the two clouds collided with each other some Myr ago, and still some of the collision signatures remain observable. The filamentary distribution in the blue cloud is parallel with each other and may indicate the collisional interaction. A similar filamentary distribution is found in the collisional layer of RCW 79 where cloud-cloud collision is suggested from CO observations (Ohama et al. 2018). A possible alternative to explain the filaments is the winds or radiation by the B stars. This scenario, however, does not explain all the filaments, some of which are not pointing toward the B star. In particular, the western most filament directed not toward the B star is not consistent with the effect of the B star.

An estimate of the collision time scale is possible by adopting a cloud size of 10 pc and a relative velocity of 4 km s^{-1} , and we obtain roughly ~ 2 Myrs as the collision duration from a ratio of the size and velocity, which gives roughly a timescale of the duration of the collisional interaction. Since the molecular gas close to the B stars are already almost fully dispersed most likely due to the ionization and winds, we assume that the collision terminated ~ 1 Myr ago, which favors the cluster age ~ 1 Myr (Pettersson & Reipurth 1994) rather than $\sim 5 \pm 4$ Myrs (Bonatto & Bica 2010). A possible

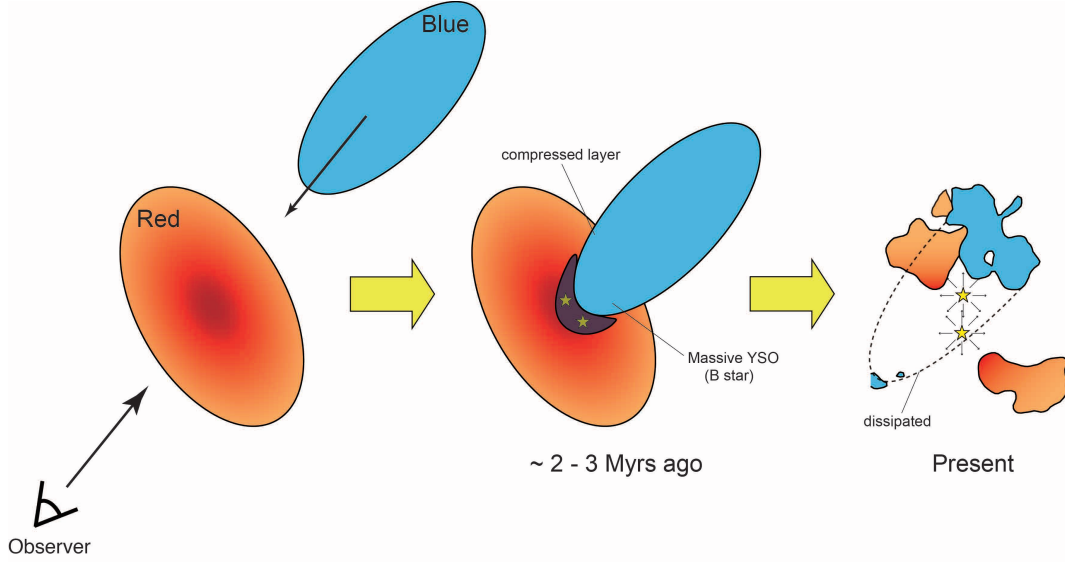


Fig. 9. Schematic image of CCC in RCW 32.

scenario is as follows; ~ 3 Myr ago the collision started, and ~ 1 Myr ago the collision ended. In the collision, the blue cloud created a cavity in the red cloud and triggered the formation of the B stars in the interface layer between the clouds were formed in 1 Myr ago (Figure 9). The B stars dispersed the natal clouds within 5 pc of these stars. The location of the blue cloud is on the near side of the HII region as evidenced by the dark lanes.

4.5.3 Triggering of the B star/cluster formation by the cloud-cloud collision?

The two signatures above characteristic to CCC suggests that collision took place in RCW 32. This does not directly support that the star formation was triggered by the CCC because the natal clouds are strongly dispersed within 5 pc of the cluster center, making it difficult to assess the natal gas properties. So, RCW 32 is a case where triggered high mass star formation is not directly confirmed based on molecular clouds due to serious cloud dispersal. This differs from a case RCW 38 where collisional triggering is firmly supported by cloud distribution thanks to a very young cluster age of 0.1 Myr (Fukui et al. 2016).

It is still possible in RCW 32 to see how the triggering scenario is feasible by using the information on the ambient gas. According to the previous samples of triggered high mass star formation, the molecular column density is as high as 10^{22} cm^{-2} for single O/early B star formation by collisional triggering (e.g., Torii et al. 2011; Fukui et al. 2016). The cloud column density of the red cloud in RCW 32 is $6 \times 10^{21} \text{ cm}^{-2}$, close to this column density. It is not excluded that the column density was as high as the threshold value in the inner dispersed part of the red cloud.

5 Conclusions

We observed molecular clouds toward RCW 32 in $^{12}\text{CO}(J = 1-0, 2-1, \text{ and } 3-2)$ and $^{13}\text{CO}(J = 1-0 \text{ and } 2-1)$ with the NANTEN2 and ASTE telescopes. The results lend support for the formation of Cr 197 including the exciting star of it through CCC. We summarize conclusions as follows.

1. We revealed that three molecular clouds are associated with RCW 32 in CO observations. The red cloud West corresponds to SFO 57 has $V_{\text{LSR}} = 2.6 - 6.8 \text{ km s}^{-1}$ and $360 M_{\odot}$, and the red cloud East corresponds to SFO 58 has $V_{\text{LSR}} = 2.6 - 6.8 \text{ km s}^{-1}$ and $900 M_{\odot}$. The blue cloud has a counterpart to the optical dark cloud in the north west of RCW 32 with $V_{\text{LSR}} = 1.4 - 3.8 \text{ km s}^{-1}$ and $300 M_{\odot}$.
2. Both the red and the blue clouds are strongly ionized by UV radiation from the exciting star(s) and show significantly high values of $R_{3-2/2-1}$ than typical galactic disk clouds.
3. We found the obvious complementary spatial distribution and connecting bridge features between the red and the blue cloud. These signatures are consistent with the collisional interaction between the clouds. We argued that the cloud distribution and kinematics are hard to explain by a simple expanding model. We present a hypothesis that a collision between the red and blue clouds took place from ~ 3 Myrs ago in a duration of ~ 2 Myrs and formed the B star(s) and the cluster whose age is ~ 1 Myr. The natal cloud dispersal is significant and we see a cavity of ~ 5 pc radius centered on the cluster. By including the previous cases of cloud-cloud collision in the VMR, e.g., , RCW 34, RCW 36, and RCW 38, an increasing number of HII region are formed by cloud-cloud collision perhaps due to the high molecular density in the region.

Acknowledgments

NANTEN2 is an international collaboration of 10 universities: Nagoya University, Osaka Prefecture University, University of Bonn, University of Cologne, Seoul National University, University of Chile, University of New South Wales, Macquarie University, University of Sydney, and University of ETH Zurich. The ASTE telescope is operated by NAOJ. The Southern H-Alpha Sky Survey Atlas (SHASSA), which is supported by the National Science Foundation. This work was financially supported by Grants-in-Aid for Scientific Research (KAKENHI) of the Japanese society for the Promotion of Science (JSPS, grant No. 15H05694). This work also was supported by Building of Consortia for the Development of Human Resources in Science and Technology of Ministry of Education, Culture, Sports, Science and Technology (MEXT, grant No. 01-M1-0305). We also acknowledge to Daiki Kurita and Ryuji Okamoto for contributions on the observations of $^{12}\text{CO}(J=3-2)$ data.

References

- Abbott, D. C. 1982, ApJ, 242, 1183
Abbott, D. C. 1982, ApJ, 259, 282
Anathpindika, S. V. 2010, MNRAS, 405, 1431

Benjamin R. A., Churchwell E., Babler B. L., et al. 2003, PASP, 115, 953

Bonatto, C., Bica, E. 2010, A&A, 516, 81

Brand, J., van der Bij, M. D. P., de Vries, C. P., et al. 1984, A&A, 139, 181

Churchwell E., Babler B., Meade M. R., et al. 2009, PASP, 121, 213

Collinder, Per 1931, AnLun, 2, 1

Crampton, D. 1972, MNRAS, 158, 85

Crampton, D., Fisher, W. A. 2010, PDAO, 516, 81

Dobbs, C. L., Pringle, J. E. & Duarte-Cabral, A., 2015, MNRAS, 446, 3608

Enokiya, R., Torii, K., Schultheis, M., et al. 2014, ApJ, 780, 72

Ezawa, H., Kawabe, R., Kohno, K., & Yamamoto, S. 2004, Proc. SPIE, 5489, 763

Ezawa, H., Kohno, K., Kawabe, R., et al. 2008, Proc. SPIE, 7012, 08

Fitzgerald, M. P., Luiken, M., Maitzen, H. M., et al. 1979, A&AS, 37, 345

Fukui, Y., Ohama, A., Hanaoka, N., et al. 2013, ApJ, 780, 36

Fukui, Y., Harada, R., Tokuda, K., et al. 2015, ApJ, 807, 4

Fukui, Y., Torii, K., Ohama, A., et al. 2016, ApJ, 820, 26

Furukawa, N., Dawson, J. R., Ohama, A., et al. 2009, ApJL, 696, L115

Gaustad J. E., McCullough P. R., Rosing W., et al. 2001, PASP, 113, 1326

Gum, C. S. 1955, Mmras, 67, 155

Habe, A., & Ohta, K. 1992, PASJ, 44, 203

Haworth, T. J., Tasker, E. J., Fukui, Y., et al. 2015, MNRAS, 450, 10

Hayashi, K., Sano, H., Enokiya, R., et al. 2017, arXiv:1706.05871

Hron, J., Maitzen, H. M., Moffat, A. F. J., et al. 1985, A&AS, 60, 355

Inoue, T., & Fukui, Y. 2013, ApJL, 774, L31

Liseau, R., Lorenzetti, D., Nisini, B., et al. 1992, A&AS, 265, 577

May, J., Murphy, D. C., & Thaddeus, P. 1988, A&AS, 73, 51

Murphy, D. C. & May, J. 1991, A&A, 247, 202

Nishimura, A., Tokuda, K., Kimura, K., et al. 2015, ApJS, 216, 18

Ohama, A., Kohno, M., Hasegawa, K., et al. 2017,

Oka, T., Onodera, Y., Nagai, M., et al. 2012, ApJS, 201, 14

Okamoto, R., Yamamoto, H., Tachihara, K., et al. 2017, ApJ, 838, 132

Onishi, T., Nishimura, A., Ota, Y., et al. 2013, PASJ, 65, 78

Pettersson, B. & Reipurth, B. 1994, A&AS, 104, 233

Ridge, N. A., Di Francesco, J., Kirk, H., et al. 2006, AJ, 131, 2921

Rodgers, A. W. 1959, Obs, 79, 49

Sano, H., Enokiya, R., Hayashi, K., et al. 2017, arXiv:1706.05763
Sorai, K., Sunada, K., Okumura, S. K., et al. 2000, Proc. SPIE, 4015, 86
Sugitani, K. & Ogura, K. 1994, ApJS, 92, 163
Sugitani, K., Fukui, Y. & Ogura, K. 1991, ApJS, 77, 59
Torii, K., Enokiya, R., Sano, H., et al. 2011, ApJ, 738, 46
Torii, K., Hasegawa, K., Hattori, Y., et al. 2015, ApJ, 806, 7
Urquhart, J. S., Thompson, M. A., Morgan, L. K., et al. 2006, A&A, 450, 625
Vogt, N. & Moffat, A. F. J. 1973, A&AS, 9, 97
Wang, Y., Jaffe, D. T., Graf, U. U., et al. 1994, ApJS, 95, 503
Yamaguchi, N., Mizuno, N., Saito, H., et al. 1999, PASJ, 51, 775
Young, J. S., Kenney, J. D., Tacconi, L., et al. 1986, ApJ, 311, 17